



# Electromagnetic Vibration of High-Voltage Line-Start Permanent Magnet Synchronous Motor with Demagnetization Fault

Cunxiang Yang<sup>1</sup> · Yiming Wang<sup>1</sup> · Hongbo Qiu<sup>2</sup> · Si Chen<sup>1</sup> · Zhenxiang Lian<sup>1</sup>

Received: 8 August 2023 / Revised: 10 January 2024 / Accepted: 21 January 2024 / Published online: 12 February 2024  
© The Author(s) under exclusive licence to The Korean Institute of Electrical Engineers 2024

## Abstract

Due to the high starting current and high temperature of the high voltage line-start permanent magnet synchronous motor, it is easy to cause partial demagnetization of the motor, which leads to increase vibration of the motor and seriously affects the operating stability of the motor. Therefore, a 10 kV, 630 kW prototype is used as an example to study the motor vibration problem caused by partial demagnetization fault. Firstly, a new method for analyzing the magnetic field variation under uniform and partial demagnetization faults is proposed. Based on this, The analytical expression for the electromagnetic force wave of HVLSPMSM under partial demagnetization is derived, and the law of electromagnetic force variation of different orders and frequencies under partial demagnetization fault is determined, while the influence of the bilateral slotted structure of the stator and rotor of the HVLSPMSM on the electromagnetic force is also considered in the derivation process. Secondly, the variation characteristics of the magnetic density trajectory are calculated by finite element method under the effects of partial demagnetization fault. It is verified that demagnetization faults cause periodic changes in the magnetic field. The harmonic content of the air-gap magnetic field and the spatial and temporal distribution characteristics of the radial electromagnetic force under uniform and partial demagnetization faults are comparatively analyzed using the finite element method. Finally, through modal analysis and harmonic response analysis, the stator vibration response characteristics caused by partial demagnetization faults are obtained, verifying the accuracy of theoretical derivation and providing a basis for the identification of motor faults.

**Keywords** Partial demagnetization · The electromagnetic force wave · Vibration

## 1 Introduction

High power factor, high efficiency and easy maintenance are the characteristics of permanent magnet motor, especially the high voltage line-start permanent magnet synchronous motor, which has the advantages of simple operation and maintenance of induction motor, but high efficiency at the same time [1–3]. High voltage line-start permanent magnet synchronous motors are the main power source for major industrial production and mining industry, and are also used as prime movers in various industries such as electric power, machinery, petrochemical, metallurgy, etc.

However, there are some shortcomings in HVLSPMSM. For example, the stator and rotor of HVLSPMSM are slotted compared to other motors, which leads to an increase in harmonic contents in the air gap, further causing increases in torque pulsation and electromagnetic vibration of the motors. At the same time, the starting current of HVLSPMSM is significantly higher than that of the induction

✉ Yiming Wang  
wangyimingwww@163.com

Cunxiang Yang  
yangzha@126.com

Hongbo Qiu  
qiu hongbohrb@163.com

Si Chen  
csmail@foxmail.com

Zhenxiang Lian  
asd369957@163.com

<sup>1</sup> College of Building Environment Engineering, Zhengzhou University of Light Industry, Zhengzhou 450002, Henan, China

<sup>2</sup> School of Electric and Information Engineering, Zhengzhou University of Light Industry, Zhengzhou 450002, Henan, China

motor of the same size, which will cause a great impact on the permanent magnet when starting, resulting in partial irreversible demagnetization, which will definitely affect the electromagnetic vibration of the motor [4–6]. Therefore, it is of great significance to study the harmonic magnetic field and electromagnetic vibration of HVLSPMSM during normal and demagnetization.

With regard to the methodology of the study of demagnetization magnetic fields, in literature [7], methods to obtain the field distributions by solving the governing field equations are also presented for machines with slots. However, the actual situation is that partial demagnetization of permanent magnets can cause the magnetic potential distributed along the circumference to partially decay in amplitude into periodic variations, which appears to cause new harmonic components to appear in the air-gap magnetism. Literature [8] presents a function reflecting the effect of demagnetization of a piece of magnet in a certain proportion around the entire air gap. This function was used in conjunction with an existing method for estimating the air-gap flux density of slotting motors to obtain the magnetic field distribution of a partial demagnetization fault. However, the method fails to derive the harmonic spatial and temporal distribution characteristics of the electromagnetic force introduced and the characteristic frequency distribution law of the vibration caused by the partial demagnetization faults.

In recent years, most of the research on demagnetization faults has focused on fault diagnosis. In literature [9], the amplitude of the side band component in frequency and the radius of gyration were selected to estimate the degree of demagnetization faults. In literature [10], a determination of the degree of demagnetization was proposed based on the d-axis and q-axis voltage variations controlled during steady-state operation of the motor. Literature [11] estimated the magnetization coefficient of the permanent magnet based on the actual measured current, voltage, and motor structure parameters to achieve monitoring of the degree of demagnetization fault. Literature [12] extracts vibration frequency-domain fault features as state indicators (CIs) for PMSM demagnetization monitoring, and then proposes a statistical diagnosis method based on Chebyshev's inequality as a method for identifying PMSM demagnetization faults. However, the temporal and spatial distribution characteristics of the electromagnetic force harmonics introduced by the asymmetry of the air-gap magnetic field caused by the partial demagnetization faults are not considered and analyzed, resulting in the inadequacy of the extracted fault feature frequencies.

There are few studies on the electromagnetic vibration of HVLSPMSM with demagnetization fault. The literature [13]

analyzed and studied the spectrum of asymmetric electromagnetic forces generated by the distortion of the air gap magnetic field in the demagnetized fault, which causes vibration and noise, and proposed a new method for detecting demagnetization faults in permanent magnet synchronous motors. Literature [14] studied the stator vibration acceleration and vibration modes under partial demagnetization and inter turn short circuit fault of PMSM. It is concluded that the radial electromagnetic force appears as a low frequency temporal and spatial harmonics under a partial demagnetization fault, which is an unbalanced magnetic pull. In literature [15], a partial demagnetization fault was simulated by cutting a single permanent magnet and replacing the cut portion with non-permanent magnet material, and it was experimentally verified that the vibration signal component is proportional to the degree of demagnetization and load torque of the permanent magnet synchronous motor. However, the above literature have not provided specific analytical calculations of the component changes of the radial electromagnetic force after partial demagnetization.

Therefore, this paper takes a 10 kV 630 kW HVLSPMSM as an example. A new method for analyzing the magnetic field variation and the spatial and temporal distribution characteristics of electromagnetic force under partial demagnetization faults is proposed. The expression of spatial and temporal distribution of radial electromagnetic force for HVLSPMSM with both slotted stator and rotor and partial demagnetization is derived by the analytical method. The harmonic contents of the air gap magnetic field and the spatial and temporal distribution of radial electromagnetic force waves are calculated by finite element method under uniform and partial demagnetization faults. The variation characteristics of the magnetic density trajectory are calculated by finite element method. Finally, the response characteristics of the stator vibration are obtained by harmonic response analysis under the demagnetization fault, verifying the accuracy of the theoretical derivation and providing a judgment basis for the identification of the motors fault.

## 2 Structural Parameters and Finite Element Model of HVLSPMSM

In this paper, a 630 kW, 10 kV HVLSPMSM is used as an example, focusing on the magnetic field variation pattern and vibration response characteristics of the motor during normal operation and partial demagnetization. A finite element model of HVLSPMSM is shown in Fig. 1. The basic parameters of the prototype are shown in Table 1.

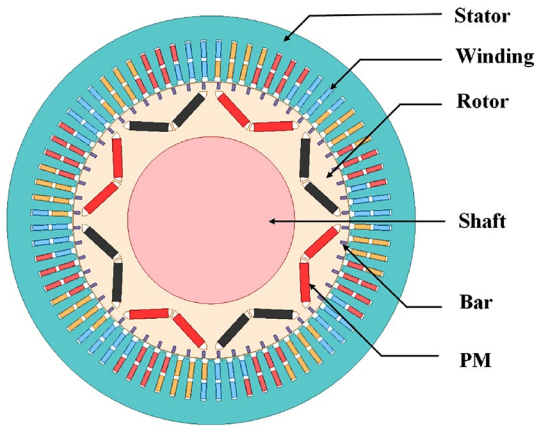


Fig. 1 Finite element model of the prototype

Table 1 Motor parameters

Parameters	Value	Parameters	Value
Stator outer diameter	880 mm	Rotor outer diameter	595 mm
Stator inner diameter	600 mm	Rotor inner diameter	360 mm
Stator slots	72	Rotor slots	56
Pole pairs	4	Connection	Y
Core length	710 mm	Rated power	630 kW
Air gap length	2.5 mm	Rated voltage	10 kV
Rated speed	750 rpm	Rated frequency	50 Hz

### 3 Radial Electromagnetic Force Wave Analysis of HVLSPMSM

#### 3.1 Analysis and Calculation of Radial Electromagnetic Force Waves in HVLSPMSM

The radial electromagnetic excitation force in the air gap is the main cause of motor vibration. The excitation force of the motor is determined by the magnetic fields of the stator and rotor, so it is essential to analyze the magnetic field.

$$B_r(\theta, t) = F_{PM}(\theta, t)\Lambda(\theta, t) \tag{1}$$

$F_{PM}(\theta, t)$  is the rotor permanent magnetomotive force(MMF) can be expressed as:

$$F_{PM}(\theta, t) = \sum_{\mu} F_{\mu} \cos(\mu\theta - \mu\omega_r t - \varphi_2) \tag{2}$$

$\Lambda(\theta, t)$  is the air gap synthetic permeability. In contrast to single-sided slotted PM motors, HVLSPMSM contains not only a constant component of air gap permeability and stator slotted permeability, but also an increased component of rotor tooth permeability, where the air gap permeability can be expressed as:

$$\Lambda(\theta, t) = \Lambda_0 + \sum_{k_1} \Lambda_{k_1} \cos k_1 Z_1 \theta + \sum_{k_2} \Lambda_{k_2} \cos k_2 Z_2 (\theta - \omega_r t) \tag{3}$$

where  $\omega_r$  is the rotor mechanical angular frequency.  $F_{\mu}$  is the  $\mu$ th harmonic MMF of the stator field,  $\mu$  is the order of the magnetomotive force (MMF) of the permanent magnet  $\mu = (2q + 1)p$ ,  $q = 0, 1, 2 \dots$   $Z_1$  represents the number of stator slots,  $Z_2$  represents the number of rotor slots,  $\Lambda_{k_1}$  represents the amplitude of the  $k_1$ th stator permeability harmonic;  $\Lambda_{k_2}$  represents the amplitude of the  $k_2$ th rotor permeability harmonic.

The radial air gap flux density during no-load operation can be expressed as Eq. (4), which shows that the slotted rotor of LSPMSM will introduce new air gap density harmonics, and the increase in the spatial harmonic contents will cause a greater degree of distortion with the air gap flux density than that of ordinary PMSM.

$$B_r(\theta, t) = \sum_{\mu} F_{\mu} \cos(\mu\theta - \mu\omega_r t - \varphi_2) \cdot \left[ \Lambda_0 + \sum_{k_1} \Lambda_{k_1} \cos k_1 Z_1 \theta + \sum_{k_2} \Lambda_{k_2} \cos k_2 Z_2 (\theta - \omega_r t) \right] \tag{4}$$

$$= \sum_{\mu} F_{\mu} \Lambda_0 \cos(\mu\theta - \mu\omega_r t - \varphi_2) + \sum_{\mu} \sum_{k_1} \frac{F_{\mu} \Lambda_{k_1}}{2} \cos[(\mu \pm k_1 Z_1)\theta - \mu\omega_r t - \varphi_2] + \sum_{\mu} \sum_{k_2} \frac{F_{\mu} \Lambda_{k_2}}{2} \cos[(\mu \pm k_2 Z_2)\theta - (\mu \pm k_2 Z_2)\omega_r t - \varphi_2]$$

New harmonics introduced by rotor slotted

The radial electromagnetic force a per unit area of the stator tooth surface can be obtained by the Maxwell stress tensor method. The tangential component of the magnetic flux density on the stator tooth surface is much smaller than the radial component when the motor in normal operation and can be ignored. The radial electromagnetic force wave  $p_r(\theta, t)$  can be obtained as:

$$p_r(\theta, t) \approx \frac{1}{2\mu_0} b_r^2(\theta, t) \tag{5}$$

The amplitude, frequency, spatial order and source of radial electromagnetic force waves can be generalized as shown in Table 2, which provides a theoretical basis for the subsequent electromagnetic vibration analysis.  $f$  is the electrical frequency.

Through the electromagnetic force wave source can be known electromagnetic force waves from three main components, where the spatial order of radial electromagnetic wave generated by the interaction of harmonic MMF of the permanent magnet and the invariant component of permeability is even multiple of the number of pole-pairs, which can be expressed as  $a = 2np$ , The frequency of each component of the electromagnetic wave is an integer multiple of

**Table 2** Radial electromagnetic force wave source, amplitude, spatial order and frequency

	Amplitude	Spatial order	Frequency
Harmonic MMF and permeability invariant component	$F_{\mu_1} F_{\mu_2} \Lambda_0^2 / 4\mu_0$	$\mu_1 \pm \mu_2$	$(\mu_1 \pm \mu_2)f$
Interaction of rotor harmonic MMF, permeability invariant component and permeability harmonics	$F_{\mu_1} F_{\mu_2} \Lambda_0 \Lambda_{k_1} / 8\mu_0$	$\mu_1 \pm \mu_2 \mp k_1 Z_1$	$(\mu_1 \pm \mu_2)f$
	$F_{\mu_1} F_{\mu_2} \Lambda_0 \Lambda_{k_2} / 8\mu_0$	$\mu_1 \pm \mu_2 \mp k_2 Z_2$	$(\mu_1 \pm \mu_2 \mp k_2 Z_2)f / p$
	$F_{\mu_1} F_{\mu_2} \Lambda_{k_{11}} \Lambda_{k_{12}} / 16\mu_0$	$\mu_1 \pm \mu_2 \pm k_{11} Z_1 \mp k_{12} Z_1$	$(\mu_1 \pm \mu_2)f$
Interaction of rotor harmonic MMF with permeability harmonics	$F_{\mu_1} F_{\mu_2} \Lambda_1 \Lambda_{k_2} / 16\mu_0$	$(\mu_1 \pm k_1 Z_1) \pm (\mu_2 \pm k_2 Z_2)$	$(\mu_1 \pm \mu_2 \mp k_2 Z_2)f / p$
	$F_{\mu_1} F_{\mu_2} \Lambda_{k_{21}} \Lambda_{k_{22}} / 16\mu_0$	$\mu_1 \pm \mu_2 \pm k_{21} Z_2 \mp k_{22} Z_2$	$(\mu_1 \pm \mu_2 \pm k_{21} Z_2 \mp k_{22} Z_2)f / p$

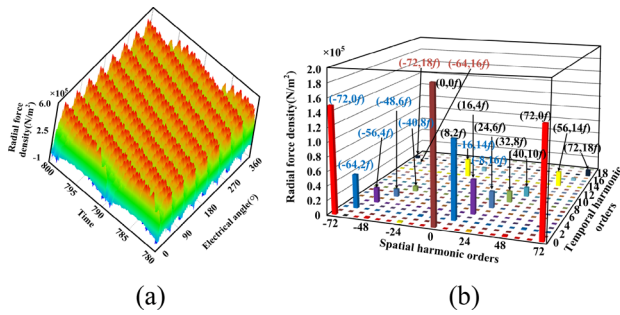


**Fig. 2** a Spatial and temporal distribution of radial electromagnetic force density. b 2D-FFT decomposition

2 times the electric frequency, so the temporal order can be expressed as  $b = 2n$ .

The spatial order of the radial electromagnetic force wave caused by the stator slotted can be expressed as  $a = 2np \pm kZ_1$ , and the temporal order is  $b = 2n$ . The spatial order of the radial electromagnetic force wave caused by the rotor slotted can be expressed as  $a = 2np \pm kZ_2$ , and temporal order are  $b = |a|/p$ . It can be seen that the stator slotted affects only the spatial distribution of the radial electromagnetic force waves without affecting the frequency characteristics, but the rotor slotted affects both the spatial distribution of the radial electromagnetic force wave and the frequency of each component.

Figure 2a shows the spatio-temporal distribution of the radial electromagnetic force wave. Figure 2b shows the spatio-temporal results of the FFT-2D. It should be noted that  $(a, bf)$  represents the harmonic density of the radial electromagnetic force wave, where the spatial order is  $a$  and the temporal order is  $b$ .  $f$  is the fundamental frequency of the stator current.

The main radial electromagnetic force wave components  $(0, 0f), (8, 2f), (16, 4f), (24, 6f), (32, 8f), (40, 10f), (48, 12f), (56, 14f), (64, 16f)$  and  $(72, 18f)$  during no-load operation can be seen from Fig. 2b to be generated by the interaction of the harmonic MMF with the permeability invariant components. Corresponding to the force wave component  $(2pn, 2nf)$  in analytical analysis. While  $(-8, 16f), (-16, 14f), (-24, 12f), (-32, 10f), (-40, 8f), (-48,$

$6f), (-56, 4f), (-64, 2f), (-72, 0)$  are generated by the stator slotted and correspond to the force wave component  $(2np \pm kZ_1, 2nf)$  in analytical analysis.  $(-72, 18f), (-64, 16f)$  is generated by the rotor slotted and corresponds to the  $(2np \pm kZ_2, |(2np \pm kZ_2)/p|f)$ . Finally, the correctness of the theoretical derivation of the spatio-temporal characteristics of the radial electromagnetic force wave was verified.

### 3.2 Analysis and Calculation of Radial Electromagnetic Force Waves after Uniform Demagnetization Faults

As shown in Fig. 3, when uniform demagnetization of all permanent magnets occurs, the resulting magnetic potential of the permanent magnets can be equated to the fact that each pair of pole permanent magnets is subjected to reverse demagnetization magnetic field, resulting in a reduction of the overall magnetic potential amplitude, but the magnetic field generated by the permanent magnets remains symmetrical. So uniform demagnetization causes a reduction in the amplitude of the magnetic potential, but does not create a new harmonic magnetic potential. Therefore, the expression of the magnetic potential of the permanent magnet under uniform demagnetization fault has only change in amplitude, the frequency and phase do not change, and no new harmonics are introduced.

### 3.3 Analysis and Calculation of Radial Electromagnetic Force Waves after Partial Demagnetization Faults

When a single permanent magnet is uniformly demagnetized, it affects the circumferential distribution of the MMF of the permanent magnet along the air gap, which further affects the spatio-temporal characteristics of the electromagnetic force. As shown in Fig. 4, when the permanent magnet is demagnetized, it can be superimposed equivalently on the normal magnetic field and the demagnetized field, This causes asymmetry of the magnetic poles, which may result in changes in the period of the air-gap magnetic potential of the permanent magnet distributed along the circumference, introducing other harmonics. So it is necessary to

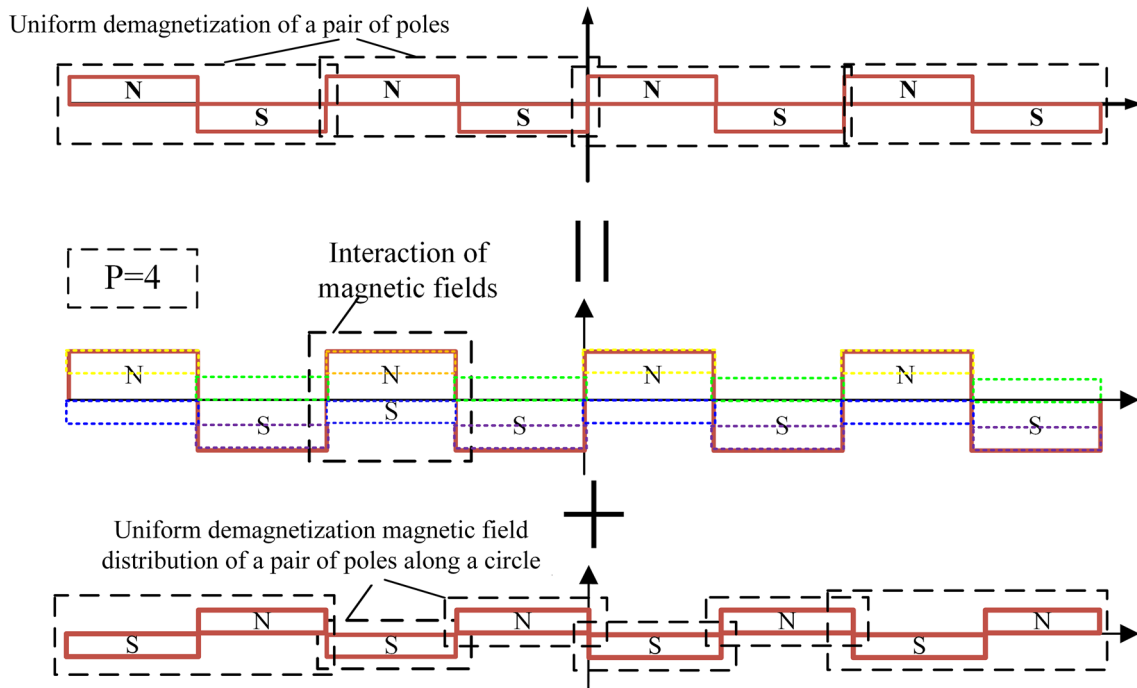


Fig. 3 Superposition of the permanent magnet field and the demagnetized field under uniform demagnetization

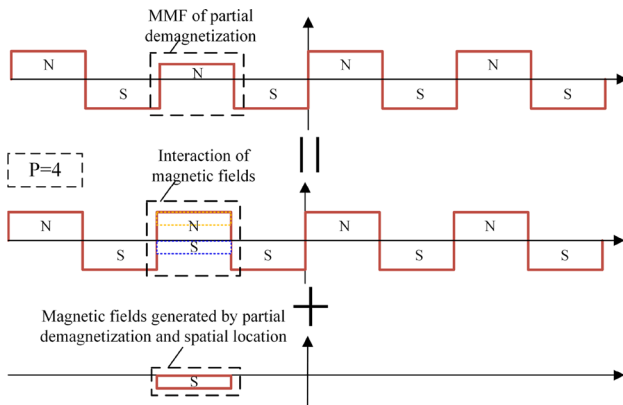


Fig. 4 Superposition of the permanent magnet field and the demagnetized field under partial demagnetization

focus on the analysis of the magnetic field distribution after demagnetization.

Figure 5 shows the equivalent magnetic field MMF distribution after a single permanent magnet is uniformly demagnetized,  $K$  is the degree of irreversible demagnetization, and  $F_{PM}/K$  is the magnitude of the MMF after demagnetization. Where  $\alpha$  is polar arc coefficient.

According to Fig. 5, the MMF distribution of the partial demagnetization permanent magnet can be written in the form of a segmented function, as shown in Eq. (6). Fourier expansion is Eq. (7).

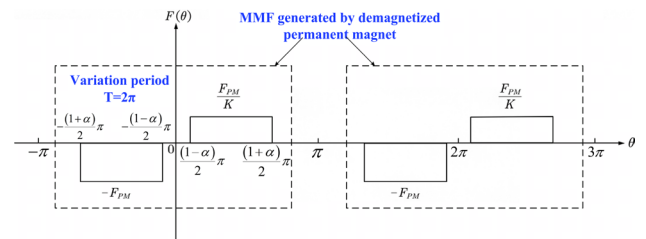


Fig. 5 MMF distribution of partially demagnetized PM

Due to the space limitation and the similarity of the spatio-temporal characteristics of the electromagnetic force generated by the action of the demagnetized magnetic field and other magnetic fields, the radial electromagnetic force wave expression when the demagnetized magnetic field acts alone is calculated by Eq. (5).

The expressions for the source, amplitude, spatial order and frequency of the additional electromagnetic force harmonics generated by the demagnetization fault are summarized in Table 3. The specific components of the radial electromagnetic force wave harmonics introduced by the partial demagnetization field in Table 4.

$$f_{PM}(\theta) = \begin{cases} -F_{PM} & -\frac{(\alpha+1)\pi}{2} \leq \theta \leq -\frac{(1-\alpha)\pi}{2} \\ 0 & -\frac{(1-\alpha)\pi}{2} < \theta \leq \frac{(1-\alpha)\pi}{2} \\ \frac{F_{PM}}{K} & \frac{(1-\alpha)\pi}{2} < \theta \leq \frac{(1+\alpha)\pi}{2} \end{cases} \quad (6)$$

**Table 3** Sources, amplitudes, spatial orders and frequencies of radial electromagnetic force waves under demagnetization

Source	Amplitude	Spatial order	Frequency
Demagnetization Harmonic MMF and permeability invariant component	$F_{n_1} F_{n_2} \Lambda_0^2 / 4\mu_0$	$n_1 \pm n_2$	$(n_1 \pm n_2)f / p$
Interaction of Demagnetization harmonic MMF, permeability invariant component and permeability harmonics	$F_{n_1} F_{n_2} \Lambda_0 \Lambda_{k_1} / 8\mu_0$	$n_1 \pm n_2 \mp k_1 Z_1$	$(n_1 \pm n_2)f / p$
	$F_{n_1} F_{n_2} \Lambda_0 \Lambda_{k_2} / 8\mu_0$	$n_1 \pm n_2 \mp k_2 Z_2$	$(n_1 \pm n_2 \mp k_2 Z_2)f / p$
	$F_{n_1} F_{n_2} \Lambda_{k_{11}} \Lambda_{k_{12}} / 16\mu_0$	$n_1 \pm n_2 \pm k_{11} Z_1 \mp k_{12} Z_1$	$(n_1 \pm n_2)f / p$
Interaction of Demagnetization harmonic MMF with permeability harmonics	$F_{n_1} F_{n_2} \Lambda_{k_1} \Lambda_{k_2} / 16\mu_0$	$n_1 \pm n_2 \pm k_1 Z_1 \mp k_2 Z_2$	$(n_1 \pm n_2 \mp k_2 Z_2)f / p$
	$F_{n_1} F_{n_2} \Lambda_{k_{21}} \Lambda_{k_{22}} / 16\mu_0$	$n_1 \pm n_2 \pm k_{21} Z_2 \mp k_{22} Z_2$	$(n_1 \pm n_2 \pm k_{21} Z_2 \mp k_{22} Z_2)f / p$

**Table 4** Components of radial electromagnetic forces generated by partial demagnetization of the magnetic field

Type of magnetic field action	Spatial order/Frequency
Demagnetization Harmonic MMF and permeability invariant component	(1, 0.25f)(2, 0.5f)(3, 0.75f)...(n, nfp)
Interaction of Demagnetization harmonic MMF, permeability invariant component and permeability harmonics	(49, 12.25f)(50, 12.5f) (51, 12.75f);(65, 1.75f) (66, 1.5f) (67, 1.25f)(68, f)(69, 0.75f)(70, 0.5f)(71, 0.25f)(73, 0.25f)(74, 0.5f)(75, 0.75f) (76, f) (77, 1.25f)...
Interaction of Demagnetization harmonic MMF with permeability harmonics	(1, 0.25f)(2, 0.5f)(3, 0.75f)...(n, nfp);(1, 54.25f)(2, 54.5f)(3, 54.75f)(4, 55f) (5, 55.25f) (6, 55.5f)(7, 55.75f)...

The bold numbers represent the number of spatial orders and temporal orders of the newly generated radial electromagnetic force after a demagnetisation fault. The bolding here is to highlight the newly generated radial EM force harmonic components

$$F_n = \frac{F_{PM} \alpha(1-k)}{4K} + \sum_{n=1}^{\infty} \left[ \frac{2F_{PM}}{n\pi} \left(\frac{1}{K} - 1\right) \cos \frac{n\pi}{2} \sin \frac{n\alpha\pi}{2} \cos n\theta + \frac{2F_{PM}}{n\pi} \left(\frac{1}{K} + 1\right) \sin \frac{n\pi}{2} \sin \frac{n\alpha\pi}{2} \sin n\theta \right]$$

Average amplitude of the magnetic potential

$$F_n = \begin{cases} F_{n=2k} = \left[ \frac{F_{PM} \alpha(1-K)}{4K} + \sum_{n=1}^{\infty} \left[ \frac{2F_{PM}}{n\pi} \left(\frac{1}{K} - 1\right) \cos \frac{n\pi}{2} \sin \frac{n\alpha\pi}{2} \cos n\theta \right] \right] \\ F_{n=2k+1} = \left[ \frac{F_{PM} \alpha(1-K)}{4K} + \sum_{n=1}^{\infty} \left[ \frac{2F_{PM}}{n\pi} \left(\frac{1}{K} + 1\right) \sin \frac{n\pi}{2} \sin \frac{n\alpha\pi}{2} \sin n\theta \right] \right] \end{cases} \quad (7)$$

$$f_{PM} = \sum_{n=1,2,3,\dots}^{\infty} F_n \cos [n(\theta - \omega_r t)] \quad (8)$$

As can be seen from Table 3, the main component of the radial electromagnetic force wave generated by partial demagnetization during no load operation is  $(n, nfp)$ , which generates a large number of low order and non-even multiples of electromagnetic force harmonics compared to normal. For example,  $(1, 0.25f)$ ,  $(2, 0.5f)$ ,  $(3, 0.75f)$ ... $(n, nfp)$  in Table 4. In general, the motor vibration displacement is approximately inversely proportional to the fourth power of the order of force waves, so the large number of lower order electromagnetic force waves generated by demagnetization will cause the motor to vibrate more.

## 4 Variation of Magnetic Field Change after Demagnetization Faults

### 4.1 Variation of Magnetic Density Waveform during Partial Demagnetization Faults

Partial demagnetization is an asymmetric demagnetization that destroys the symmetry of the magnetic density distribution and has a significant impact on motor performance. In order to determine the pattern of magnetic field changes after demagnetization, waveforms of the magnetic density at different locations on the core of the motor are obtained by numerical calculations, meaning the variation of the magnetic density values and the variation of the radial Br and tangential Bt components of the magnetic density with time.

As can be seen from Fig. 6a, the stator teeth tips are magnetically saturated and the overall magnetic density of the stator teeth is greater than that of the stator yoke. Therefore, in this paper, taking the two points A and B of the stator core teeth and the stator yoke of the motor at the zero moment of demagnetization fault of the permanent magnet space position, as shown in the Fig. 6b.

Since the change rule of magnetic density waveforms at point A and B is the same, only the flux change at point B of the stator yoke during the mechanical cycle is selected. As

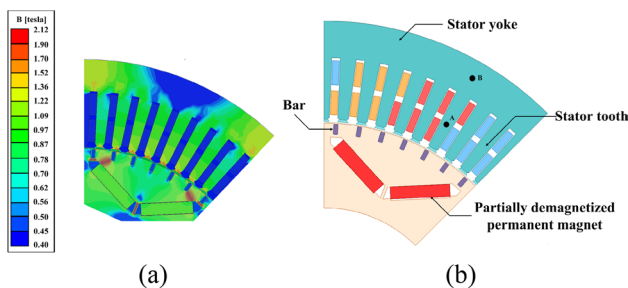


**Fig. 6** a Magnetic density cloud map. b Magnetic density reference point and faulty permanent magnet position at zero moment

shown in Fig. 7, the magnetic density wave at point B varies periodically with time under the normal working conditions of the PM, and the amplitude is basically the same. When the permanent magnet has different degrees of demagnetization fault, the most obvious change in flux density waveform is amplitude oscillation, and the amplitudes in different periods are no longer equal. When the fault permanent magnet is far away from the magnetic density reference point B, the oscillation degree of the magnetic density amplitude decreases. At half-rotation of the motor, the magnetic density at point B rises, but not at the same amplitude as normal operation. The amplitude oscillation of the magnetic density becomes more intense as the single permanent magnet faults of the

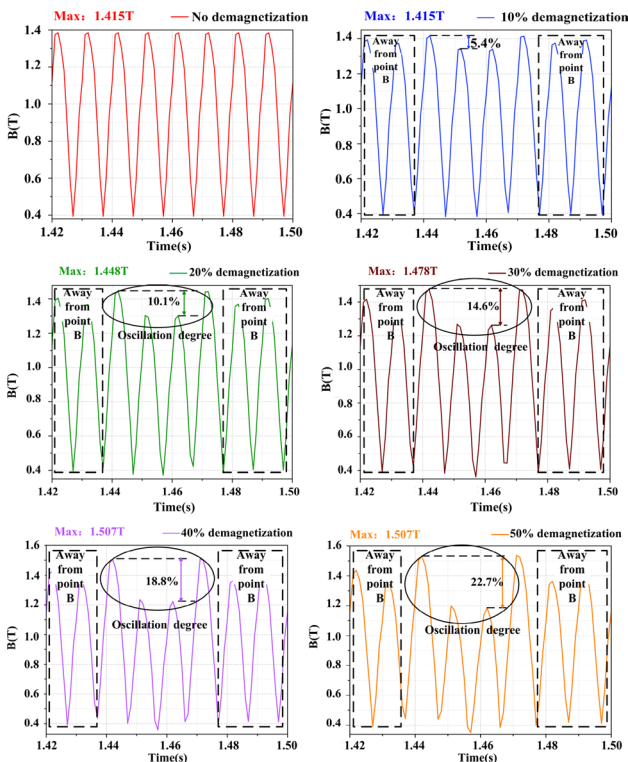


**Fig. 7** Variation of magnetic density at point B with time for different degrees of uniform demagnetization

rotor increases. The peak amplitude oscillations of demagnetization are 5.4, 10.1, 14.6, 18.8 and 22.7% respectively.

The rotational path of the  $B_r$  and  $B_t$  components of the magnetic density at points A and B. The magnetic field diagrams are obtained for the motor at point A and B when the permanent magnets are normal and at different degrees of demagnetization.

As can be seen from Fig. 8, when the permanent magnet is normal, the amplitude of the  $B_r$  and  $B_t$  components of the magnetic density does not change. So the distribution of the magnetic field in each cycle almost follows the same path. After the demagnetization fault occurs, the magnetic field does not repeat the same path. In addition, the radius of magnetic density trajectory during the fault is larger than the radius in the healthy, and increases gradually as demagnetization fault intensifies. The change in the path of the magnetic density trajectory is caused by fluctuations in the radial and tangential components of the magnetic density. The periodicity of the path change needs to be analyzed.

In order to investigate the exact period of change in the magnetic density trajectory after demagnetization, the magnetic density trajectories at points A and B under normal operation and with 50% partial demagnetization are selected for comparison.

Figure 9a shows the trajectory changes of point A and point B between 0.4–0.42 s and 0.42–0.44 s in the same

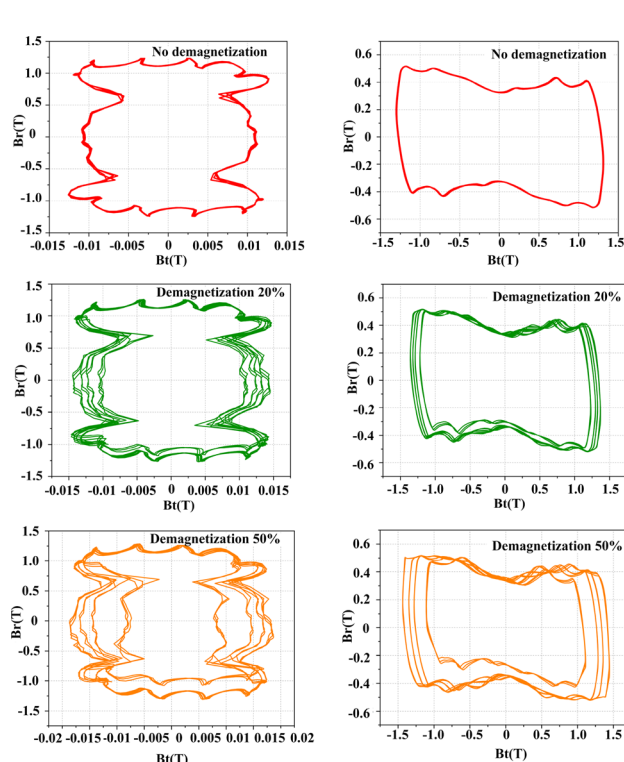


**Fig. 8** Trajectory of partial demagnetization at points A (left) and B(right)

electrical cycle  $T = 0.02\text{s}$  without demagnetization. It can be clearly seen that the magnetic field generated by the permanent magnets is distributed almost along the same path, so that the magnetic field period does not change in the no demagnetization.

Figure 9b shows the path of points A and B at 50% partial demagnetization within the same electrical period  $T = 0.02\text{s}$  at  $(0.4\text{ s}, 0.42\text{ s})$  and  $(0.42\text{ s}, 0.44\text{ s})$ , which shows that the magnetic field is not symmetrical and the magnetic density trajectory period changes. Figure 9c shows the magnetic density path of point A and point B at 50% partial demagnetization within  $(0.4\text{ s}, 0.48\text{ s})$  and  $(0.48\text{ s}, 0.56\text{ s})$ , and it can be seen that the paths are almost the same within  $0.08\text{ s}$ , so the magnetic density path change period after partial demagnetization is  $0.08\text{ s}$ .

In summary, the asymmetric distribution of the magnetic field after demagnetization causes the electrical

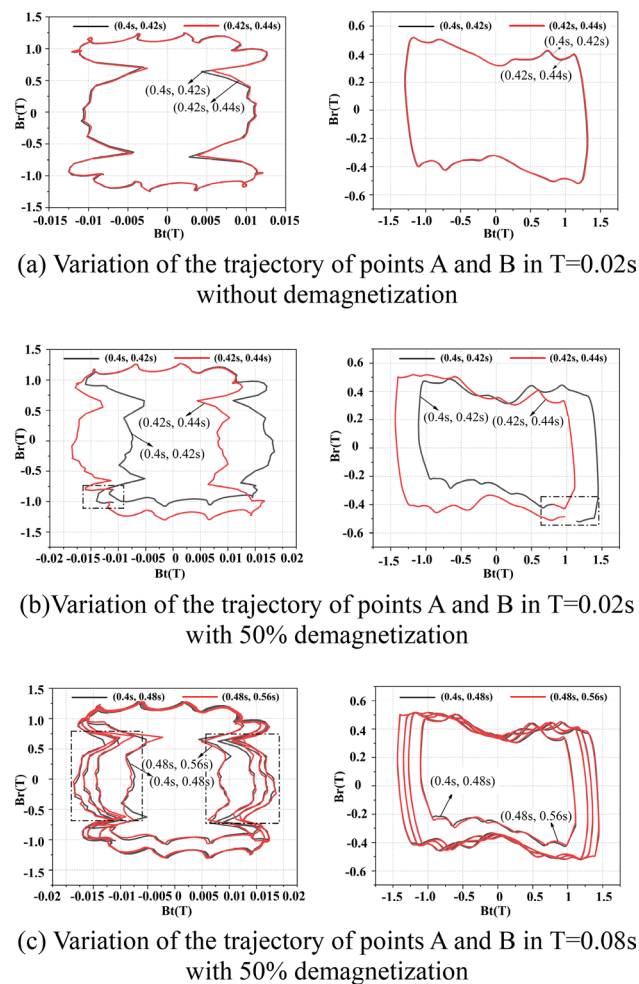


**Fig. 9** Variation of the cycle of the trajectories in points A and B. **a** Variation of the trajectory of points A and B in  $T = 0.02\text{ s}$  without demagnetization. **b** Variation of the trajectory of points A and B in  $T = 0.02\text{ s}$  with 50% demagnetization. **c** Variation of the trajectory of points A and B in  $T = 0.08\text{s}$  with 50% demagnetization

period of the partial magnetic density trajectory to become  $T = 0.08\text{s}$ , the harmonic period generated by the demagnetized magnetic field becomes  $T = 0.08\text{s}$ .

## 4.2 Variation of the Air Gap Magnetic Density during Uniform Demagnetization Faults

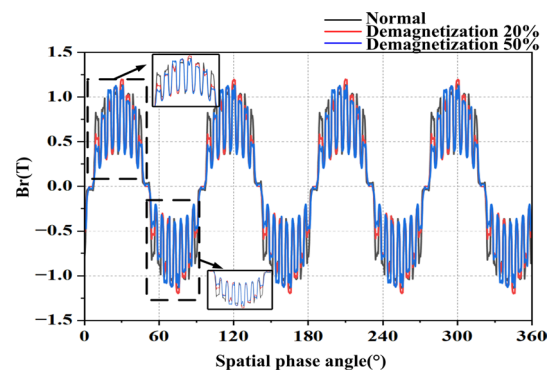
After the motor is started at no load, the air gap magnetic density is generated by the permanent magnets of the rotor. When permanent magnets have irreversible demagnetization, it will inevitably affect the waveform of the magnetic field and its magnitude.

Figure 10 shows a comparison of the spatial distribution of air-gap magnetic density for no demagnetization, 20% uniform demagnetization and 50% uniform demagnetization. It can be seen that due to the stator and rotor are grooved, resulting in the air gap magnetism is not smooth, but the overall distribution is sinusoidal. The eight peaks in the diagram represent the eight poles. The dotted line box in the figure corresponds to the change of the magnitude of the air gap magnetism under a pair of poles, and it can be seen that with the increase of the degree of uniform demagnetization, the overall magnitude of the air gap magnetism decreases, but it does not result in the distortion of the air gap magnetism.

Figure 11 shows the harmonic components of the air gap magnetism at different degrees of uniform demagnetization. It can be seen that the uniform demagnetization fault leads to a large reduction in the amplitude of each harmonic component of the air gap magnetism, but the harmonic components remain unchanged.

## 4.3 Variation of the Air Gap Magnetic Density during Partial Demagnetization Faults

A radar plot of the spatial distribution of the air-gap magnetic density for different degrees of demagnetization



**Fig. 10** Comparison of air gap magnetic with different degrees of uniform demagnetization



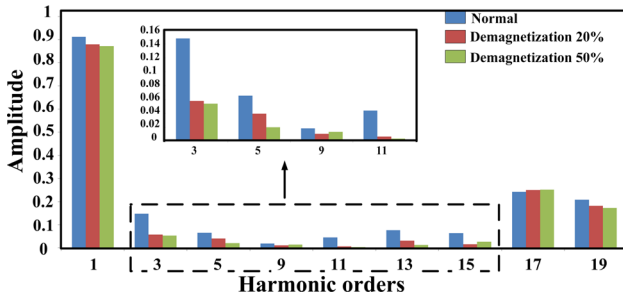


Fig. 11 Harmonic orders of the air gap magnetic density for different degrees of uniform demagnetization

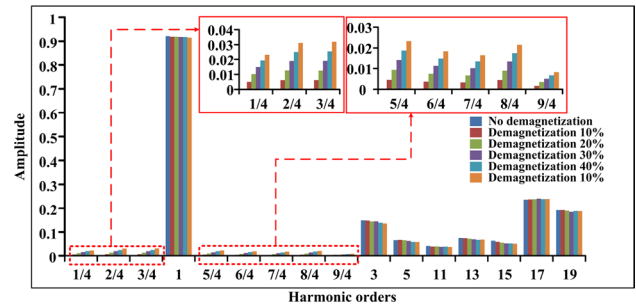


Fig. 14 Harmonic orders of the air gap magnetic density for different degrees of partial demagnetization

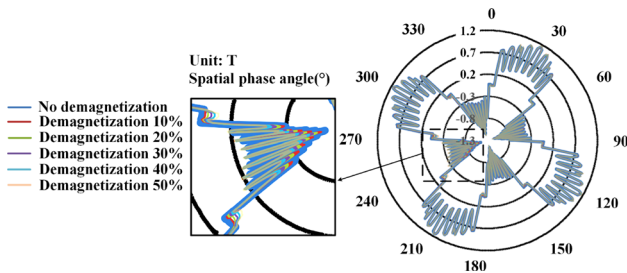


Fig. 12 Radar map of the spatial distribution of the air gap magnetic density

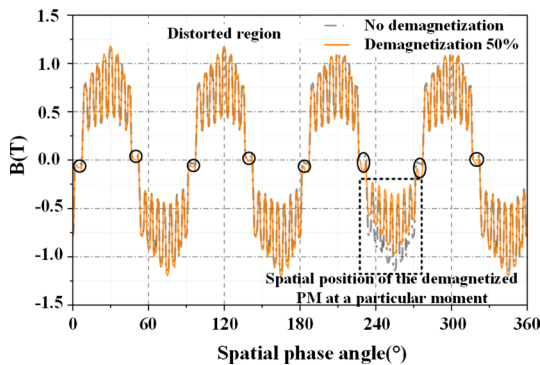


Fig. 13 Comparison of air gap magnetic with no demagnetization and 50% demagnetization

within 0.08 s of a mechanical cycle of the motor is shown in Fig. 12. The waveform of the magnetic density of the air gap at a certain time without demagnetization and with 50% partial demagnetization is also compared, as shown in Fig. 13.

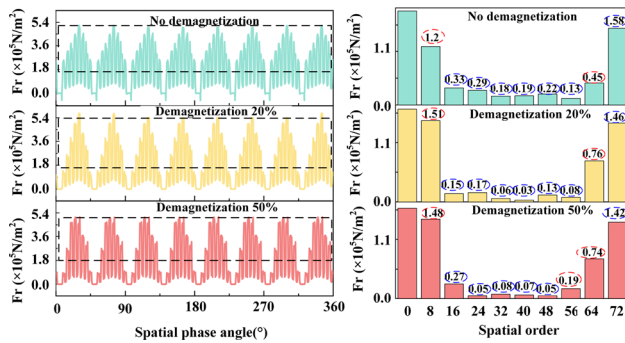
In Fig. 12, it can be easily seen that there are four pairs of poles in the motor, and when no partial demagnetization fault occurs, the air gap density is symmetrically distributed along the circumference. After the partial demagnetization fault occurs, there is an overall decrease in the magnitude of the magnetic density at a certain spatial position where the demagnetized permanent magnet is located, and the airgap magnetic density is not symmetrically distributed.

In the rectangular frame of Fig. 13, the air gap density is significantly reduced. This is due to the uniform demagnetization of the corresponding piece of permanent magnet at this location, which results in an overall reduction in the air gap magnetic density in this region, thus affecting the symmetry of the air gap density. As demagnetization increases, the peak value of the air-gap magnetic density increases and the curve is not smooth. This is due to a single permanent magnet demagnetization fault that causes the air gap magnetic field to become asymmetrical and increases the harmonic contents.

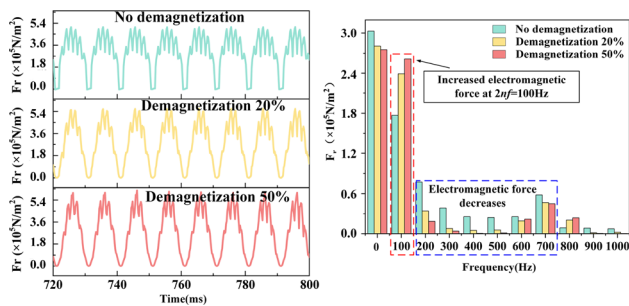
From these two figures, it can be seen that the effect of uniform demagnetization of a single permanent magnet on the air-gap magnetic density is related to the spatial position. The number of air gap magnetic density harmonics (the ratio of the number of harmonic pole pairs in the air gap to the number of main wave poles) is given by Fast Fourier Transform for different demagnetization faults.

Figure 14 shows the air-gap magnetic density harmonic decomposition under partial demagnetization faults. When the motor has no demagnetization, the harmonic content of the 1st, 3rd, 5th, 9th, 17th and 19th harmonics within the air gap magnetic field is higher, where the 17th and 19th harmonics are the 1st tooth harmonics of the motor. The amplitude of the newly introduced  $k/p$ -th harmonics increases with the degree of demagnetization. The increase in harmonic content and amplitude will not only have an effect on the electromagnetic performance of the motor, but also on the electromagnetic forces generated by the interaction between the air-gap magnetic density and the multiple harmonics will increase the vibration of the motor.

The comparison of the waveforms of the air-gap magnetic density and the changes in the harmonic components of the air-gap magnetic density with the two types of demagnetization faults verify the accuracy of the theoretical analysis in Sect. 3, which further illustrates that the uniform demagnetization fault has a symmetrical distribution of the magnetic field, and that the partial demagnetization fault destroys



**Fig. 15** Spatial distribution and spatial order of radial electromagnetic forces for uniform demagnetization



**Fig. 16** Temporal distribution and frequency of radial electromagnetic forces with for uniform demagnetization

the original periodicity of the air-gap magnetic density and introduces new harmonic components.

#### 4.4 Spatial and Temporal Distribution of Radial Electromagnetic Forces under Uniform Demagnetization Faults

Radial electromagnetic force wave forms are generated by finite element simulations at varying degrees of demagnetization, both along the circumference of the air gap and at specific points in time. Spatial and temporal characteristics are then demonstrated by FAST Fourier Transform analysis.

According to Figs. 15 and 16 in the radial electromagnetic force temporal distribution and spatial distribution of waveforms can be seen, uniform demagnetization caused by radial electromagnetic force amplitude fluctuations and does not introduce new harmonics.

Figure 15 shows the distribution of radial electromagnetic force waves along the circumference of the air gap at a certain moment in time for different levels of uniform demagnetization faults. The black boxed area in the waveform graph shows the spatially distributed waveform amplitude fluctuations. As the degree of uniform demagnetization increases, the amplitude fluctuations become larger.

At 50 per cent uniform demagnetization, the RMS value is  $2.35 \times 10^5 \text{ N/m}^2$ , a decrease of 7.2 per cent. In the Fourier transform of the spatial domain, The red dashed line indicates the increase in radial electromagnetism of spatial order after uniform demagnetization. The blue dashed line indicates that the radial electromagnetic force of the spatial order decreases after uniform demagnetization. It can be seen that uniform demagnetization does not break the symmetry of the radial electromagnetic space, introduces harmonics and only affects the magnitude of the radial electromagnetic force.

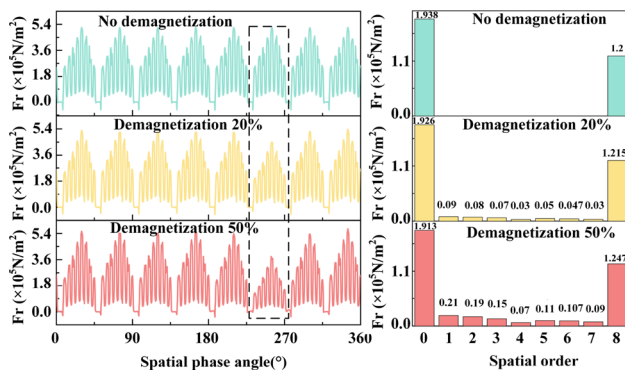
Figure 16 shows the waveform and Fourier spectrum of the radial electromagnetic force at a particular point under varying degrees of uniform demagnetization. In the time domain of the Fourier transform can be obtained, uniform demagnetization causes an increase in radial electromagnetic force at 2 times the frequency out, where the radial radial electromagnetic force at 20% of uniform demagnetization is  $2.39 \times 10^5 \text{ N/m}^2$ , an increase of 35.8%. The radial EMF at 50% uniform demagnetization is  $2.61 \times 10^5 \text{ N/m}^2$ , an increase of 48.2%. The radial electromagnetic force at each frequency in the blue dashed box decreases as the degree of homogeneous demagnetization increases. So the uniform demagnetization does not affect the distribution characteristics of the radial electromagnetic force in the time domain and still satisfies the spatio-temporal characteristics of the radial electromagnetic force ( $2pn, 2nf$ ).

#### 4.5 Spatial and Temporal Distribution of Radial Electromagnetic Forces under Partial Demagnetization Faults

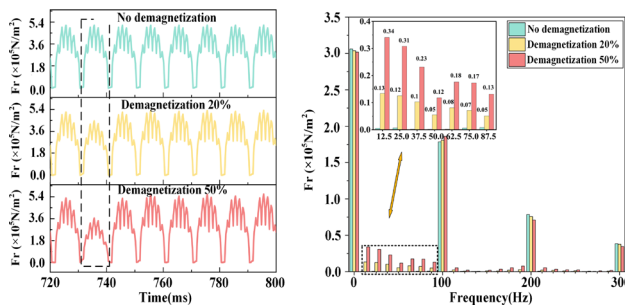
According to Figs. 17 and 18, the demagnetized position causes a decrease in the magnetic density of the air gap, which in turn causes a decrease in the radial electromagnetic force at that position. In addition, any increase in the harmonic content of the air gap magnetic density will affect the harmonic component of the radial electromagnetic force.

Figure 17 shows the distribution of radial electromagnetic force waves along the circumference of the air gap at a certain moment in time for different levels of partial demagnetization and FFT results. In general, the motor vibration displacement is approximately inversely proportional to the fourth power of the number of force waves, so the first eight spatial orders are selected, which have a greater influence on vibration. It can be seen that, as the degree of demagnetization increases, the radial electromagnetic force wave at the demagnetized position gradually decreases, while a new spatial harmonic is introduced with a harmonic spatial order of  $n$  ( $n = 1, 2, 3, \dots$ ). This is consistent with the results of the analytical calculations. The amplitude of the introduced harmonic increases as the degree of demagnetization.

Figure 18 shows the waveform and Fourier spectrum of the radial electromagnetic force at a particular point under



**Fig. 17** Spatial distribution and spatial order of radial electromagnetic forces for partial demagnetization



**Fig. 18** Temporal distribution and frequency of radial electromagnetic forces for partial demagnetization

varying degrees of partial demagnetization. It is evident that partial demagnetization of a single permanent magnet can affect the temporal variation of the radial electromagnetic force. The mechanical period of the motor is 0.08 s, and the time required to pass this point remains constant over one week of rotation. Therefore, a single permanent magnet demagnetization fault results in a fluctuation of the radial electromagnetic force wave over a mechanical period. These fluctuations gradually increase as the degree of demagnetization worsens. At the same time, additional harmonics are introduced, including fractions of the fundamental frequency such as  $1/4, 2/4, 3/4 \dots n/p$ , and their amplitudes gradually increase as the magnetization decreases. Moreover, the newly introduced harmonic frequencies correspond to theoretical calculations. And the fractional frequency harmonics produced by the action of the demagnetized magnetic field increase the possibility of resonance.

In summary, this study investigated the spatial and temporal distribution of radial electromagnetic force waves caused by partial demagnetization faults. Finite element calculations have been used to conclude that partial

**Table 5** Material parameters of stator

Name	Material	Density (kg/m <sup>3</sup> )	Elastic Modulus	Poisson's ratio
Stator	Silicon steel	7800	152GPa	0.27

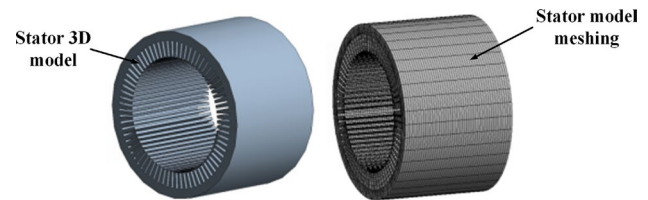


**Fig. 19** Stator Modelling and Mesh Sections

demagnetization leads to imbalanced magnetic pull and generates numerous low order spatial harmonics and fractional frequency time harmonics.

## 5 Modal Analysis

When the frequency of the radial electromagnetic force harmonics is approximately or exactly the same as the natural frequency of the motor stator, resonance occurs, resulting in a higher vibration response. Therefore, modal analysis is a key step in the study of electromagnetic vibration in electric motors. Through modal analysis, we can clearly understand the modal vibration pattern of each order of the motor stator structure and its inherent frequency, and analyze the possibility of resonance in electric motors.

### 5.1 3D Model Building and Finite Element Meshing

Based on the mechanical parameters of the high-voltage self-starting permanent magnet synchronous motor, a 3D model of the stator was drawn and imported into Ansys Workbench for modal solving. Silicon steel sheets are used for the stator core and their material parameters are shown in Table 5.

The role of meshing is to discretise a complex model into finite-cell solution domain problems. The stator selects the automatic mesh method for swept mesh or tetrahedral mesh delineation. The finite element meshing of the stator is shown in Fig. 19.

### 5.2 Solution for Modal Analysis of Stator

In this paper, the modal solution is carried out for the stator core using finite elements. The first six orders of the natural frequency of the stator core are shown in Fig. 20. It can be seen from the figure that the frequency increases with the order of the radial mode, but the gap between the frequencies of two adjacent orders decreases. It shows that at low order modes there is a large difference between the natural frequencies, but at higher order there is less difference between the natural frequencies, therefore at higher order there is a higher probability of resonance in the motor. High voltage motors are generally larger in size, and the longer outer diameter of the stator core results in a lower natural frequency of the stator, which should be focused on the low and medium frequency bands of vibration.

## 6 Harmonic Response Analysis

On the basis of air gap magnetic density, radial electromagnetic force wave and structural modal analysis, a magneto-solid coupling model for electromagnetic vibration studies is established to calculate the electromagnetic vibration response characteristics of HVLSPMSM.

Based on the density of electromagnetic force calculated by ANSYS Maxwell from the stator electromagnetic grid to the structural grid, unidirectional coupling of the magnetic field to the structure is achieved and the electromagnetic vibration of the motor is calculated by harmonic response.

Figure 21 shows the vibration acceleration spectrum without demagnetization, where the vibration acceleration amplitude has spikes at  $2f$ ,  $4f$ ,  $6f$ ,  $8f$ ,  $10f$  and  $12f$  respectively, these frequencies are  $2nf$ , and it can be seen from the previous figure that the amplitude of electromagnetic force at these frequency points is larger and causes a more pronounced vibration response. In addition to the larger magnitude at  $2nf$ , there is also significant vibration at 325,

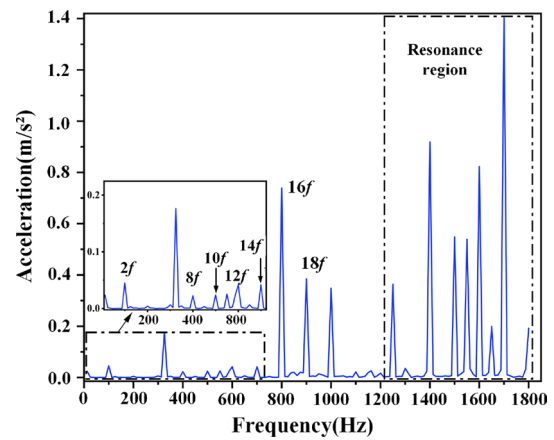


Fig. 21 Vibration acceleration spectrum under normal

1250, 1550 and 1650 Hz, which is due to the increase in frequency components caused by the default period selected when the finite element performs harmonic calculations, which is very small for the amplitude of the stress wave, but close to the intrinsic frequency causing resonance, so the acceleration amplitude is larger. Significant acceleration increases at  $16f=800$  Hz and  $18f=900$  Hz. Due to the fact that  $16f$  corresponds to a spatial order of 8, which is the smallest non-zero spatial order radial electromagnetic force wave in this prototype 8-pole motor, and its corresponding vibration pattern is the 8th order vibration pattern, as shown in Fig. 22.

The spatial order of  $18f$  electromagnetic force is 72. According to the stator tooth modulation theory, when the force wave order is greater than  $Z_p/2$ , the higher order electromagnetic force wave will be modulated to lower order electromagnetic force, and the modulated electromagnetic force order is  $\lambda-nZ$ . Therefore, the 72-order electromagnetic force in the air gap of the 72-slot 8-pole motor studied in this paper is modulated by 72 teeth to zero-order electromagnetic force, which causes zero-order vibration

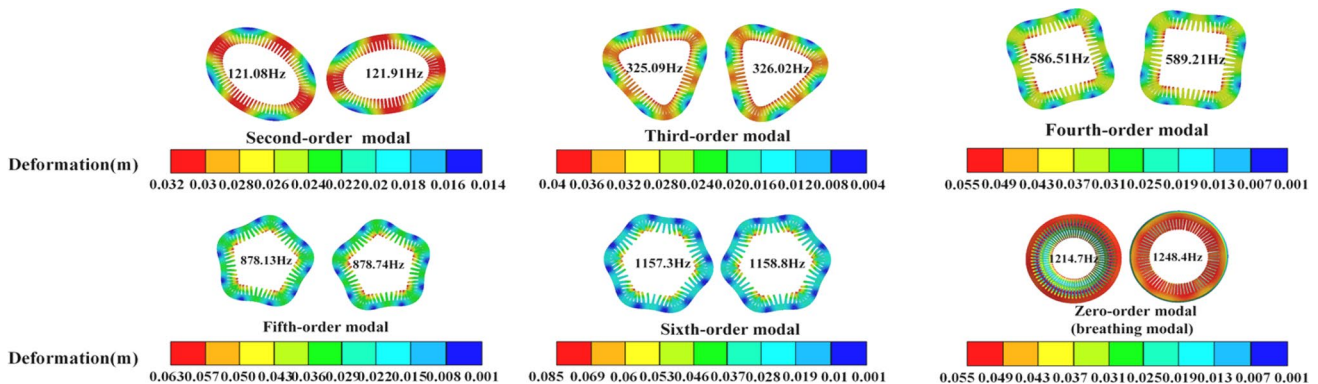


Fig. 20 Mode shape with corresponding to natural frequency

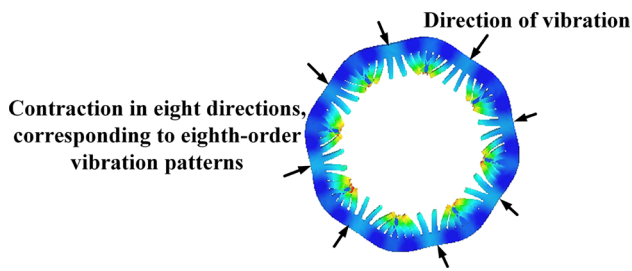


Fig. 22 16f corresponding vibration pattern

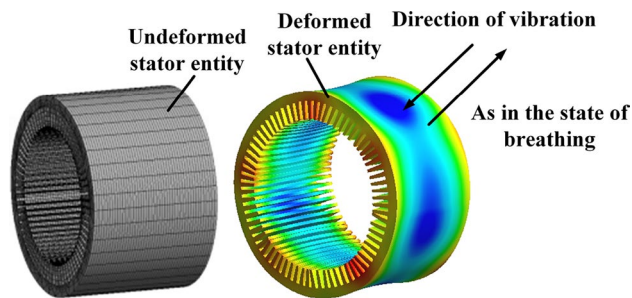


Fig. 23 18f corresponding vibration pattern

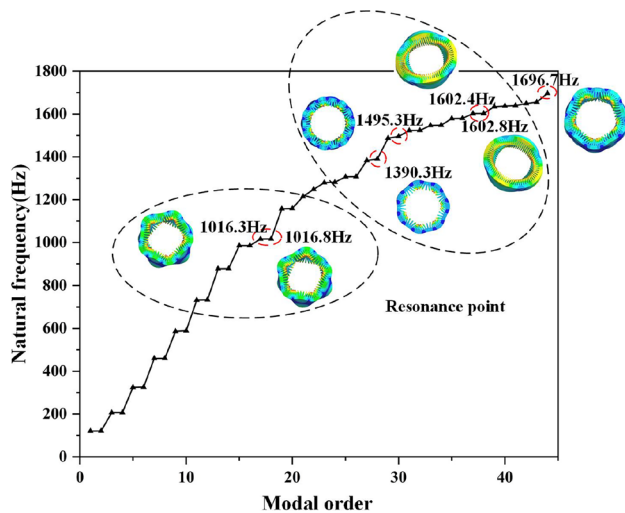


Fig. 24 First 50th order modal natural frequencies

of the stator yoke. The vibration pattern corresponding to 18f is shown as the 0th order vibration pattern in Fig. 23.

Figure 24 shows the natural modal frequencies of the stator up to 1700 Hz. At speed of 750 rpm, the radial electromagnetic force is even multiples at  $20f = 1000$  Hz,  $28f = 1400$  Hz,  $30f = 1500$  Hz,  $32f = 1600$  Hz and  $34f = 1700$  Hz. Although the amplitude of the radial electromagnetic force wave in this part is small, it is close to the natural frequency of the motor and causes resonance,

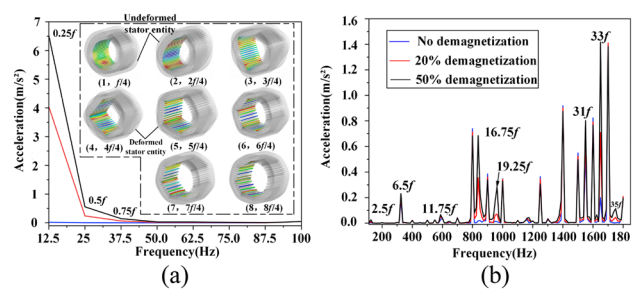


Fig. 25 a Vibration acceleration spectrum in 100 Hz and corresponding vibration patterns. b Vibration acceleration spectrum from 200 to 1800 Hz

resulting in increased vibration. The resonant frequencies point are indicated by the red boxes in the diagram.

Figures 25 shows the amplitude of vibration acceleration for normal, 20% partial demagnetization, and 50% partial demagnetization. It indicates that there is no significant difference in vibration amplitude at  $2nf$  before and after demagnetization. But the electromagnetic forces close to the intrinsic frequency, which leads to a sudden surge in vibration amplitude that increases with the degree of demagnetization.

From the two figures, it can be seen that the electromagnetic forces introduced into the motor after demagnetization at non-even multiples of  $0.25f$ ,  $2.5f$ ,  $6.5f$ ,  $11.25f$ ,  $16.25f$  and  $19.25f$  produce significant vibration. The frequencies of the electromagnetic forces are consistent with the law of  $nf/p$  ( $p = 4$ ,  $f = 50$  Hz) and the time harmonic components of partial demagnetization of electromagnetic forces derived in Sect. 3.

Figure 25a shows the three types of vibration acceleration spectra up to 100 Hz and their corresponding vibration patterns. It can be seen that the vibration amplitude is greatest at  $0.25f$  when the motor is demagnetied, and the increases with the degree of demagnetization. The vibration pattern of the stator can be seen to correspond to the radial electromagnetic force wave ( $n$ ,  $nf/p$ ).

Figure 25b shows the three types of vibration acceleration spectra from 200 to 1800 Hz. It can be seen that the additional vibration acceleration surges are all due to the  $nf/p$  frequency component introduced by partial demagnetization, where  $6.5f = 325$  Hz coincides with the second order natural frequency,  $11.75f = 587.5$  Hz is close to the fourth order intrinsic frequency, and  $31f = 1550$  Hz is close to the eighth order natural frequency. It can be seen that partial demagnetization can cause vibrations that are not even multiples of the fundamental frequency, and can be violent at  $0.25f$ . The amplitude of vibration at even multiples of the fundamental frequency decreases slightly with increasing demagnetization.

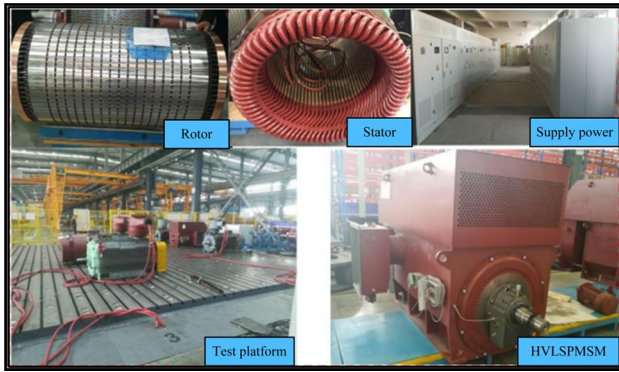


**Fig. 26** Prototypes and experimental platform

**Table 6** Comparison of the finite element calculation results and the experimental value of the experimental value about HVLSPMSM

Comparison parameter	Test data	Calculated results	Variation rate (%)
Rated load current	38.5 A	38.4 A	0.26
Efficiency	0.981	0.986	0.50
EMF	5.024 kV	5.39 kV	7.28
No load current	6.6 A	6.57 A	0.45
Copper loss	5.87 kW	5.70 kW	2.90

## 7 Experimental Tests and Result Analysis

In order to verify the accuracy of the model, the prototype is tested by experimental platform as show in Fig. 26. The experimental platform includes dynamometer machine, power analyzer, industrial condensing unit, DSP data acquisition system and other experimental equipment. Motor in the rated voltage, rated frequency no-load operation to reach a stable state, adjust the motor's applied terminal voltage, so that its no-load current is minimum, record the test motor's outgoing terminal voltage  $U_{ab}$ ,  $U_{ac}$ ,  $U_{bc}$ , and take the average value as the no-load counter electromotive force voltage value. The motor is operated at rated frequency and rated voltage and load is applied to the motor at six load points. Starting from the maximum load, two points are selected uniformly between the 100 and 150% load points, as well as the 100, 75, 50, and 25% load points, and the voltage, current, and power are measured and load characteristic curves are obtained.

The experimental data of the current, power factor, efficiency and loss are obtained through the prototype test platform when the prototype is working at no load and rated load. The experimental data are compared with the finite element model calculated results, as shown in Table 6.

It can be seen from Table 6 that the errors of the model are less than 8% at different operating conditions. The calculated results are in good agreement with the experimental data at different operating conditions. The accuracy of the model is verified.

## 8 Conclusion

In this paper, an analytical method is proposed for the analysis of magnetic density and electromagnetic force by equating the magnetic potential generated by the partial demagnetization and uniform demagnetization to a decrease in amplitude distributed along the circumference.

The results obtained in the investigation show that the main component of the radial electromagnetic force wave generated by partial demagnetization is  $(n, nf/p)$   $n \in Z$  about HVLSPMSM. While uniform demagnetization does not introduce new harmonics of the radial electromagnetic force and only affects the magnitude of the radial electromagnetic force. This is due to the partial demagnetization of a permanent magnet changes the period of its resulting permanent magnet magnetic potential distributed along the circumference, which in turn generates an even number of permanent magnet harmonic magnetic potentials, affecting the temporal and spatial distribution characteristics of the electromagnetic force, and verified by finite element analysis.

The results obtained in the investigation show that the vibration amplitude of HVLSPMSM is greatest at  $0.25f$  in the low frequency band after partial demagnetization, and increases with the degree of demagnetization. The vibration patterns of the stator can be seen to correspond to the radial electromagnetic force wave  $(n, nf/p)$ , This result reaffirms the accuracy of the proposed methodology for the study of demagnetization faults and the derivation of electromagnetic forces.

To complete this study, several areas can be next considered, such as: the effect of unilateral magnetic pulling force on the vibration of the rotor due to the asymmetry of the air gap magnetic density caused by partial demagnetization faults in HVLSPMSM; The effect of thermal stress deformation on motor vibration due to irreversible demagnetization caused by an increase in the temperature of the permanent magnets in HVLSPMSM.

**Acknowledgements** This work was supported in part by the National Natural Science Foundation of China under Grant [52177063], [U2004183] and in part by Excellent Young Scholars Project of Henan Province under Grant [232300421070], and in part by the University Science and Technology Innovation Talent Support Program of Henan province under Grant [23HASTIT026], and in part by the Science and technology project of Henan Province under Grant [232102220080].

## References

1. Waheed A, Kim B, Cho YH (2020) Optimal design of line-start permanent magnet synchronous motor based on magnetic equivalent parameters. *J Electr Eng Technol* 15:2111–2119
2. Jędryczka C, Knypiński Ł, Demenko A, Sy-kulski JK (2018) Methodology for cage shape optimization of a permanent magnet synchronous motor under line start conditions. *IEEE Trans Magn* 54(3):1–4
3. Yan B, Wang X, Yang Y (2018) Comparative parameters investigation of composite solid rotor applied to line-start permanent-magnet synchronous motors. *IEEE Trans Magn* 54(11):1–5
4. Kurihara K, Rahman MA (2004) High-efficiency line-start interior permanent magnet synchronous motors. *IEEE Trans Ind Appl* 40(3):789–796
5. Liu X, Huang S (2016) Magnetic field and thrust analysis of the U-channel air-core permanent magnet linear synchronous motor. In: 2016 IEEE conference on electromagnetic field computation (CEFC), Miami, FL, USA, pp 1–1
6. Moghadam DE, Speck J, Grossmann S, Stahl J (2018) Voltage distribution in the stator windings of high voltage motors fed by PWM drives part I: effects of the pulse characteristics. In: 2018 IEEE 2nd international conference on dielectrics (ICD), Budapest, Hungary, pp 1–4
7. Gyftakis K, Garcia-Calva T, Skarmoutsos G, Morinigo-Sotelo D, Mueller M, Romero-Troncoso RJ (2021) Detection and identification of demagnetization in PM generators during transient conditions. In: IEEE 13th international symposium on diagnostics for electrical machines, power electronics and drives (S-DEMPED), vol 1, pp 345–350
8. Sengupta S, Endla N, Kushwaha A, Fernandes BG (2023) Modelling and analysis of PM demagnetization and its effect on vibration in SPM machines. In: 2023 IEEE 14th international symposium on diagnostics for electrical machines, power electronics and drives (S-DEMPED), Chania, Greece, pp 377–382
9. Ebrahimi BM, Faiz J (2013) Demagnetization fault diagnosis in surface mounted permanent magnet synchronous motors. *IEEE Trans Magn* 49(3):1185–1192
10. Haddad RZ, Lopez CA, Foster SN, Strangas EG (2017) A voltage-based approach for fault detection and separation in permanent magnet synchronous machines. *IEEE Transact Ind Appl* 53(6):5305–5314
11. De Bisschop J, Abdallah A, Sergeant P, D-upré L (2014) Identification of demagnetization faults in axial flux permanent magnet synchronous machines using an inverse problem coupled with an analytical model. *IEEE Trans Magn* 50(11):1–4
12. Xing M, Ding H, Ren X, Wang T, Ge S, Shen J (2021) On the accuracy of rotor demagnetization fault detection in PMSM using vibration-based condition indicators. In: 2021 CAA symposium on fault detection, supervision, and safety for technical processes (SAF-EPROCESS), Chengdu, China, pp 1–6
13. Torregrossa D, Khoobroo A, Fahimi B (2012) Prediction of acoustic noise and torque pulsation in PM synchronous machines with static eccentricity and partial demagnetization using field reconstruction method. *IEEE Trans Ind Electron* 59(2):934–944
14. Yang Z, Shi X, Krishnamurthy M (2014) Vibration monitoring of PM synchronous machine with partial demagnetization and inter-turn short circuit faults. In: 2014 IEEE transportation electrification conference and expo (ITEC), Dearborn, MI, USA, pp 1–6
15. Ishikawa T, Igarashi N (2019) Failure diagnosis of demagnetization in interior permanent magnet synchronous motors using vibration characteristics. *Appl Sci* 9(15):3111

**Publisher's Note** Springer Nature remains neutral with regard to jurisdictional claims in published maps and institutional affiliations.

Springer Nature or its licensor (e.g. a society or other partner) holds exclusive rights to this article under a publishing agreement with the author(s) or other rightsholder(s); author self-archiving of the accepted manuscript version of this article is solely governed by the terms of such publishing agreement and applicable law.



**Cunxiang Yang** He received the Ph.D. degree in electrical engineering from the Southeast University, in 1996. His research interests include electromagnetic and thermal analysis on electrical machine, especially in permanent magnetic machines.



**Yiming Wang** He is working toward the M.S. degree in electrical machines at Zhengzhou University of Light Industry. His research interests include electromagnetic and vibration analysis, especially in high-voltage line-starting permanent magnet motor.



**Hongbo Qiu** He received the Ph.D. degree in electrical engineering from the Harbin University of Science and Technology, in 2014. His research interests include electromagnetic and thermal analysis on electrical machines, especially in permanent magnetic machines.



**Si Chen** He is working toward the M.S. degree in electrical machines at Zhengzhou University of Light Industry. His research interests include electromagnetic and vibration analysis, especially in high-voltage line-starting permanent magnet motor.



**Zhenxiang Lian** He is working toward the M.S. degree in electrical machines at Zhengzhou University of Light Industry. His research interests include electromagnetic and vibration analysis, especially in high-voltage line-starting permanent magnet motor.